SCIENCE CHINA
Technological Sciences

• Article •

April 2022 Vol. 65 No. 4: 966–976
https://doi.org/10.1007/s11431-021-1970-8

Lagrangian coherent structures and their heat-transport mechanism in the turbulent Rayleigh-Bénard convection

CHENG Hang[1], SHEN Jie[1], ZHANG YiZhao[1], ZHOU Quan[1], CHONG Kai Leong[1], LIU YuLu[1,2] & LU ZhiMing[1*]

[1] *Shanghai Institute of Applied Mathematics and Mechanics, Shanghai Key Laboratory of Mechanics in Energy Engineering and School of Mechanics and Engineering Science, Shanghai University, Shanghai* 200072*, China;*
[2] *The School of Sciences, Shanghai Institute of Technology, Shanghai* 200072*, China*

Received September 24, 2021; accepted November 23, 2021; published online February 21, 2022

In this paper, we investigate the Lagrangian coherent structures (LCSs) and their heat-transport mechanism in turbulent Rayleigh-Bénard (RB) convection. Direct numerical simulations (DNS) are performed in a closed square cell with Rayleigh numbers (Ra) ranging from 10^6 to 10^9 and Prandtl (Pr) number fixed at $Pr = 0.7$. First, our results show the power-law relationship between Nusselt number (Nu) and Ra, $Nu = 0.99Ra^{0.30\pm0.02}$, confirming the results from previous studies. To gain insights into the material transport, LCSs are extracted using the finite-time Lyapunov exponent (FTLE) method. Interestingly, lobe structures are widely present, and we elucidate their role in transporting heat from the corner rolls to large-scale circulation. Next, the relationships between LCSs and thermal plumes are examined, and we identify two behaviors of thermal plumes: first, most plumes transport along the LCSs; second, few plumes are exposed to the bulk and subsequently mix with the turbulent background. Furthermore, we quantify the heat flux along the LCSs, which contributes to about 85% of the total flux regardless of Ra. This suggests that LCSs play a significant role in heat transport. Finally, the viscous (thermal) dissipation rate along the LCSs is quantified, which is larger than 80% (60%) of the total value, suggesting that LCSs are responsible for the large viscous and thermal dissipations.

Rayleigh-Bénard convection, finite-time Lyapunov exponent, Lagrangian coherent structures

Citation: Cheng H, Shen J, Zhang Y Z, et al. Lagrangian coherent structures and their heat-transport mechanism in the turbulent Rayleigh-Bénard convection. Sci China Tech Sci, 2022, 65: 966–976, https://doi.org/10.1007/s11431-021-1970-8

1 Introduction

Turbulent thermal convection is omnipresent in natural and industrial processes, such as atmospheric circulation [1], oceanic movement [2], and electronic equipment [3]. The paradigm to study thermal convection is the classical Rayleigh-Bénard (RB) convection, which is a fluid layer heated from below and cooled from above [4–6]. An important issue in RB convection is heat transport, and a good understanding of its mechanism is necessary to advance the efficiency of engineering applications.

The heat transfer efficiency in RB convection is usually controlled by two dimensionless parameters: Rayleigh number (Ra) and Prandtl number (Pr). The response of RB convection is characterized by the global heat and momentum transport which can be expressed as the Nusselt number (Nu) and Reynolds number (Re), respectively. The scalings of the Nu and Re on Ra and Pr have been extensively studied over the past years by experiments [7–9], numerical simulations [10–12], and theories [5, 13, 14]. For example, the Grossmann-Lohse (GL) theory [14] has been proposed as a unifying theory for effective scaling in RB convection and successfully predicts how Nu and Re depend on Ra and Pr

*Corresponding author (email: zmlu@shu.edu.cn)

over a wide parameter range. Additionally, the geometry of the cell is relevant as well. For more details, we refer the readers to the recent studies [15–18].

Coherent structures in RB convection play an essential role in heat transport [19–26]. Several methods have been proposed to extract coherent structures based on the Eulerian perspective, such as the Q-criteria [27], proper orthogonal decomposition (POD) [28–30], and dynamic mode decomposition (DMD) [31, 32]. Typical examples of coherent structures in RB convection are thermal plumes, large-scale circulation, and corner-flow rolls. The thermal plumes are the primary heat carriers in turbulent thermal convection. They are ejected from the thermal boundary layers (BLs) and then self-organized to form large-scale circulation. Large-scale circulation has also been studied on its formation [21], movement [24], stagnation [25], reversal [26], coupling with the corner-flow rolls, and effects on heat transport. For instance, Huang et al. [33] revealed that the competition between corner-flow rolls and large-scale circulation leads to anomalous Nu-Pr relations in the quasi-two-dimensional (2D) RB convection at $Pr \approx 2$–3 for moderate Ra.

Although the Eulerian method for coherent structure extraction has been widely used, there are limitations on showing the spatial-temporal evolution of coherent structures [34, 35]. Recently, investigations of the coherent structures from the Lagrangian perspective have attracted significant attention [36–40]. In contrast to the traditional Eulerian analysis, the Lagrangian perspective gained insight into the dispersion of fluid elements [41]. Several heuristic and mathematical detection methods have been developed to identify the coherent structures from the Lagrangian perspective [37], such as the finite-time Lyapunov exponent (FTLE) [42], dynamic Laplace operator method [43], and Lagrangian-averaged vorticity deviation (LAVD) [44]. FTLE has been widely used as an objective and robust Lagrangian method to identify the flow structures in turbulent flows. This method was first proposed by Haller and Yuan [42] to properly define the boundaries of Lagrangian coherent structure (LCSs). In their following studies, they enriched the LCSs theory [34, 45–48] and defined the ridges in the FTLE fields as LCSs [49, 50]. Revealing the LCSs extracted from flow data is useful in understanding the material transport and mixing events. Shadden et al. [40] employed the FTLE method to study the processes of entrainment and detrainment of materials by looking at the so-called lobe structures. Green et al. [34] used the FTLE method to identify LCSs in three-dimensional turbulent flows. They showed the evolution of a single hairpin vortex into a hairpin packet. He et al. [51] analyzed the evolution of LCSs in a cylinder-wake disturbed flat plate BL and extracted the mean convective velocity and average inclination angle of LCSs. Li et al. [52] obtained the characteristics and transport properties of LCSs in the turbulent channel flow through spatial-temporal correlation analysis. The Lagrangian approach has also been used to analyze RB convection [36, 53]. Schneide et al. [53] used the FTLE method to identify LCSs in turbulent RB convection with different integration times. However, the investigation of the relationship between LCSs and heat transport has received less attention.

In this paper, we employ the FTLE method to study the LCSs in RB convection, and their effects on heat transport are explored. It is hoped that the new information on the LCSs can help to understand the mechanism of heat transport and deepen the insights into the coherent structures in RB convection.

The remainder of the paper is organized as follows. Section 2 briefly describes the numerical and analytical methods, and the results and discussion are presented in Section 3. Finally, Section 4 presents the conclusion.

2 Numerical and analytical methods

2.1 Numerical methods-DNS

In the Oberbeck-Boussinesq (OB) approximation, the dimensionless governing equations for the dynamics of RB convection are given by

$$\begin{aligned} &\nabla \cdot \boldsymbol{u} = 0, \\ &\frac{\partial \boldsymbol{u}}{\partial t} + (\boldsymbol{u} \cdot \nabla)\boldsymbol{u} = -\nabla p + \sqrt{\frac{Pr}{Ra}}\nabla^2 \boldsymbol{u} + \theta \hat{\boldsymbol{z}}, \\ &\frac{\partial \theta}{\partial t} + (\boldsymbol{u} \cdot \nabla)\theta = \sqrt{\frac{1}{RaPr}}\nabla^2 \theta, \end{aligned} \tag{1}$$

where $\boldsymbol{u}(u, w)$, θ, and p are the velocity, temperature, and kinematic pressure fields, respectively, and $\hat{\boldsymbol{z}}$ is the vertical unit vector. No-slip boundary conditions for the velocity fields are employed at all solid walls. For temperature, adiabatic boundary conditions were used for vertical sidewalls. The top and bottom plates are fixed at constant dimensionless temperatures $\theta = -0.5$ and $\theta = 0.5$, respectively. Two control parameters in the RB convection: The Rayleigh number (Ra) and Prandtl number (Pr) are defined as follows:

$$Ra = \frac{\alpha g \Delta H^3}{\nu \kappa}, \quad Pr = \frac{\nu}{\kappa}, \tag{2}$$

where α, ν, and κ are the thermal expansion coefficient, kinematic viscosity, and thermal diffusivity of the fluid, respectively; Δ is the temperature difference across the fluid layer of height H; and g is the acceleration due to gravitation. The response parameters for turbulent RB convection are expressed in terms of the Nusselt number (Nu), which is expressed as follows:

$$Nu = \sqrt{RaPr}\,\langle w\theta \rangle - \langle \partial\theta/\partial z \rangle, \tag{3}$$

where w is the vertical component of the velocity, and $\langle\cdot\rangle$ denotes the average overtime and any horizontal line.

We conduct direct numerical simulations (DNS) of the turbulent RB convection in a square box of height H spanning $10^6 \le Ra \le 10^9$. All simulations are conducted at fixed $Pr = 0.7$, corresponding to a working fluid of air [54]. We use the fourth-order finite-difference scheme with staggered grids to solve the governing equations. The grid spacing is uniform in horizontal and vertical directions. The number of grid points increases from 256×256 to 1024×1024 as Ra increases from 10^6 to 10^9. The resolution has been chosen to resolve the BLs and smallest scale of the turbulent flow. The thermal BLs are resolved with at least 16 grid points for all runs. Details of the grid resolution and flow parameters for these simulations are given in Table 1. We note that the measured Nu is consistent with Zhang et al. [55] to a precision of less than 1%. Bao et al. [56] used the same code as ours to calculate the enhancement of heat transport in partitioned thermal convection. Their simulations yield similar results to the experiments for small numbers of partitions. Additionally, our simulation code has been well validated and adopted by Chen et al. [57] and Zhang et al. [15,58].

2.2 Analytical methods-FTLE

The definitions of FTLE method are given by Haller and Yuan [42] and Shadden et al. [50]. According to the definitions, a flow map function denoted by $\varphi_{t_0}^t$ satisfies

$$\varphi_{t_0}^t : \boldsymbol{x}_0 \mapsto \varphi_{t_0}^t(\boldsymbol{x}_0) = \boldsymbol{x}(t; t_0, \boldsymbol{x}_0), \tag{4}$$

where $\boldsymbol{x}_0$ is an initial particle distribution that is advected by the flow at time t_0, and this point moves to $\varphi_{t_0+T}^t$ after a time interval T, as shown in Figure 1. To describe the amount of stretching about this trajectory, we consider the evolution of the perturbation point $\boldsymbol{y}_0 = \boldsymbol{x}_0 + \delta\boldsymbol{x}(0)$, where $\delta\boldsymbol{x}(0)$ is infinitesimal and arbitrarily oriented. The perturbation after a time interval T then becomes

$$\delta\boldsymbol{x}(t_0+T) = \varphi_{t_0}^{t_0+T}(\boldsymbol{y}_t) - \varphi_{t_0}^{t_0+T}(\boldsymbol{x}_t) = \frac{\mathrm{d}\varphi_{t_0}^{t_0+T}(\boldsymbol{x})}{\mathrm{d}\boldsymbol{x}}\delta\boldsymbol{x}(t_0) + O(\|\delta\boldsymbol{x}(t_0)\|^2), \tag{5}$$

where $O(\|\delta\boldsymbol{x}(t_0)\|^2)$ is the infinitesimal amount of Taylor series expansion of the flow about point $\boldsymbol{x}$, which can be ignored here. The FTLE value is obtained from the following equation:

$$\sigma_{t_0}^T = \frac{1}{T}\ln\sqrt{\lambda_{\max}(\Delta)}, \tag{6}$$

where $\lambda_{\max}$ is an operator that returns the largest eigenvalue of the symmetric matrix.

$$\Delta = \frac{\mathrm{d}\varphi_{t_0}^{t_0+T}(\boldsymbol{x})^*}{\mathrm{d}\boldsymbol{x}}\frac{\mathrm{d}\varphi_{t_0}^{t_0+T}(\boldsymbol{x})}{\mathrm{d}\boldsymbol{x}}, \tag{7}$$

Δ is a finite-time version of the (right) Cauchy-Green deformation tensor, and $\frac{\mathrm{d}\varphi_{t_0}^{t_0+T}(\boldsymbol{x})^*}{\mathrm{d}\boldsymbol{x}}$ denotes the adjoint of $\frac{\mathrm{d}\varphi_{t_0}^{t_0+T}(\boldsymbol{x})}{\mathrm{d}\boldsymbol{x}}$.

The ridges of FTLE fields given by eq. (6) represent the LCSs at a finite-time interval T from x_0. If the integration time of the FTLE method calculation is positive ($T > 0$), the ridges indicate repelling LCSs. In contrast, if the integration time is negative ($T < 0$), the ridges indicate the location of attracting LCSs.

One question this study faces is how the integration time T should be selected. If T is too small, the critical LCSs may not be identified. In contrast, if T is too large, more flow details are generated, making it difficult to identify the critical LCSs. In this paper, we take the large-scale circulation turnover time $t_E := 4\pi/\langle|\omega_c(t)|\rangle_t$ (ω_c denotes the center vorticity) [59] as the characteristic time-scale. Five different integration times T ($t_E/4, t_E/2, t_E, 3t_E/2$, and $2t_E$) are then compared, and the results show that for $T \ge t_E/2$, the contour maps of FTLE fields are similar. Considering the accuracy of the results, we selected t_E as the integration time T (refer to Table 1). The forward time is used to identify the repelling

Table 1 Simulation parameters. $N_x \times N_z$ denotes the resolution in horizontal and vertical directions

Pr	Ra	$N_x \times N_z$	Nu	Re	t_E
0.7	1×10^6	256×256	6.31	276	8.4
0.7	3×10^6	384×384	7.64	470	6.8
0.7	1×10^7	512×512	11.42	1033	6.9
0.7	3×10^7	720×720	16.54	1782	6.5
0.7	1×10^8	720×720	25.29	3623	6.3
0.7	3×10^8	768×768	35.86	6883	5.3
0.7	5×10^8	896×896	42.48	9413	4.6
0.7	1×10^9	1024×1024	51.51	15551	2.8

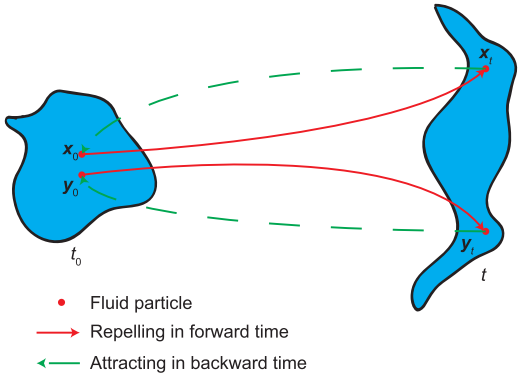

Figure 1 Sketch of Lagrangian evolution of material points in backward and forward time. The solid red line represents the sketch of the repelling motions of fluid particles in the forward time; the dotted green line represents the sketch of the repelling motions of fluid particles in the backward time.

LCSs in RB convection, which will be discussed further in Section 3.2.

3 Results and analysis

Using the numerical and analytical methods presented in the previous section, we first analyze the typical flow structures in RB convection from the Eulerian perspective, as shown in Section 3.1. Section 3.2 then presents the analysis of LCSs and their effects on heat transport from the Lagrangian perspective.

3.1 Eulerian coherent structures

In Figure 2(a) and (b), we show the typical snapshots of the instantaneous velocity fields (arrows), and the corresponding temperature fields (color) obtained from the simulations with $Pr = 0.7$ and $Ra = 10^8$ and 10^9, respectively. As shown in Figure 2, there is a large-scale circulation with several smaller secondary rolls at the corners [55, 60]. With increasing Ra, the large-scale circulation shifts from a tilted (nearly) elliptical shape at $Ra = 10^8$ to a circular shape at $Ra = 10^9$.

As Ra increases, the thermal buoyancy of the system increases, changing the flow structure. To examine this change, Figure 3(a) and (b) show the horizontal profiles of the time-averaged vertical velocity $\langle w(x)\rangle_t$ and temperature $\langle\theta(x)\rangle_t$ obtained at the mid-height of RB convection cell for various Ra. It is seen that the peak velocities become larger and the peak location gets closer to the sidewall, signaling thinner viscous BLs, with increasing Ra. The positive peak of the vertical velocity (refer to Figure 3(a)) is associated with the upward moving hot fluid (refer to Figure 3(b)). The magnitudes of the vertical velocity increase as Ra increases, whereas the magnitudes of temperature decrease. This is because, as Ra increases, the plumes enter the bulk region more often (refer to Figure 2(b)).

Further, we will analyze the local Nu distribution for different Ra. Figure 4(a) shows the measured local heat flux $\langle Nu(x)\rangle_t/Nu$ as a function of x at the mid-height for different Ra. Here, the formula for Nu is given in eq.(3). It can be seen that for all Ra, the local heat flux exhibits a pronounced peak near the sidewall. Additionally, the peak magnitudes of the local heat flux increase with Ra. Figure 4(b) shows a log-log plot of the measured Nu as a function of Ra. The data can be well described by a power law relationship, and the dashed line shows the best fit given by $Nu = 0.99Ra^{0.30\pm0.02}$. This scaling is consistent with the previous numerical results for 2D convection cells [55].

3.2 Lagrangian coherent structures

In order to have a comprehensive understanding of the coherent structures in RB convection, we use the FTLE method to identify the coherent structures in the Lagrangian framework,

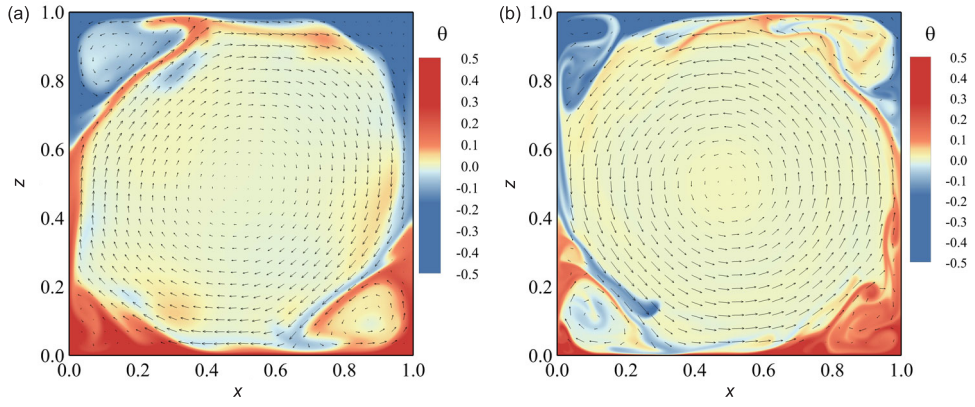

Figure 2 Typical snapshots of the instantaneous flow fields for (a) $Ra = 10^8$ and (b) 10^9. The magnitudes of velocity and temperature are coded in arrows and color, respectively.

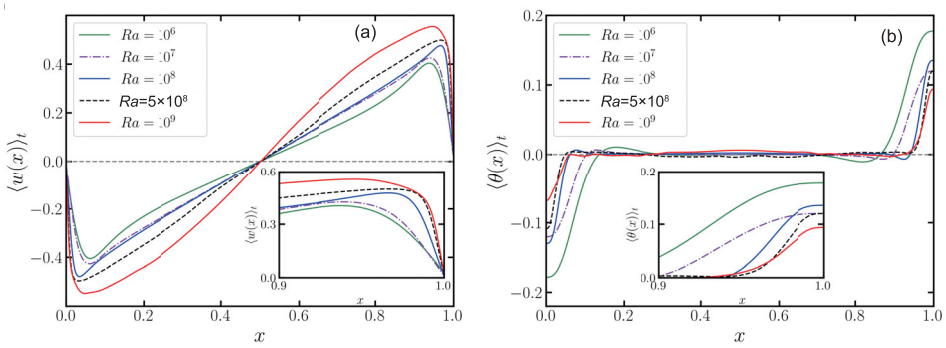

Figure 3 The time-averaged horizontal profiles of the vertical velocity and temperature. The time-averaged horizontal profiles of (a) the vertical velocity $\langle w(x)\rangle_t$ and (b) temperature $\langle \theta(x)\rangle_t$ obtained at the mid-height of a 2D convection cell at different Ra. The insets are zooms of the upper-plate region to reveal the near-wall behaviors.

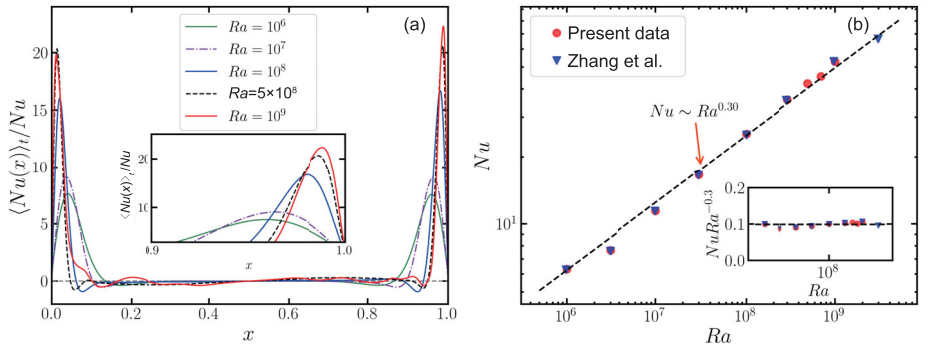

Figure 4 (a) Normalized local heat flux $\langle Nu(x)\rangle_t/Nu$ obtained at the mid-height of a convection cell for various Ra. The inset is a zoom in the right-plate region to reveal the near-wall behaviors. (b) Ra-dependence of Nu, and Nu and Ra in log-log plot. The dashed lines represent the best power law fits to the corresponding data. The insets show the compensated plots $NuRa^{-0.3}$ versus Ra.

where the FTLE fields are obtained from velocity fields using the method introduced in the preceding section.

Theoretically, the LCSs are recognized as the ridges of the FTLE fields. However, it is difficult and laborious to locate the ridges from FLTE fields. Shadden et al. [50] identified the LCSs according to the criterion: FTLE $> c$, where c is a given threshold. This method relies on experience, and the selection of the threshold depends on the particular problem. Following the concept of identifying plumes in RB convection, LCSs are defined as the regions with $\mathrm{FTLE}(x,y) - \langle \mathrm{FTLE}\rangle_x > c\mathrm{FTLE}_{\mathrm{r.m.s.}}$. Here, c is a given threshold. After our verification, the empirical threshold is set to be $c = 1.2$. Figure 5(a) shows a typical FTLE field at $Ra = 10^9$. Figure 5(b) and (c) show the LCSs identified from FTLE fields using Shadden et al.'s method and our method, respectively. It can be seen that the LCSs extracted using the two methods are similar, and they capture the main structures (or skeleton) of FTLE fields. A careful comparison between the LCSs obtained using the two methods shows that our method includes more flow structures than the Shadden et al.'s method.

Figures 6 and 7 show the snapshots of LCSs at $Ra = 10^8$ and 10^9, respectively, illustrating the difference between the evolution of LCSs at different Ra. Additionally, Figures 6 and 7 show the flow and temperature fields at the same instant for comparison. As shown in Figure 6, the large-scale circulation is surrounded by LCSs, the boundaries of which vary slightly within a large-scale circulation period. This indicates that the fluid in the large-scale circulation can only weakly mix with the surroundings. Interestingly, many lobe structures exist in the corner and sidewall regions. However, such lobe structures cannot be realized from the flow and temperature fields (see left panel of Figure 6(a)–(d)). To depict the roles of lobe structures in RB convection, particular attention should be paid to those structures in the corner-flow roll. As shown in Figure 6(a), the hot fluid which detaches from the thermal BL is first trapped in the lobe structure (refer to the position indicated by the green arrow in the blue frame of Figure 6). As time evolves (refer to Figure 6(b) and (c)), the hot fluids in the lobe structure are conducted from the corner-

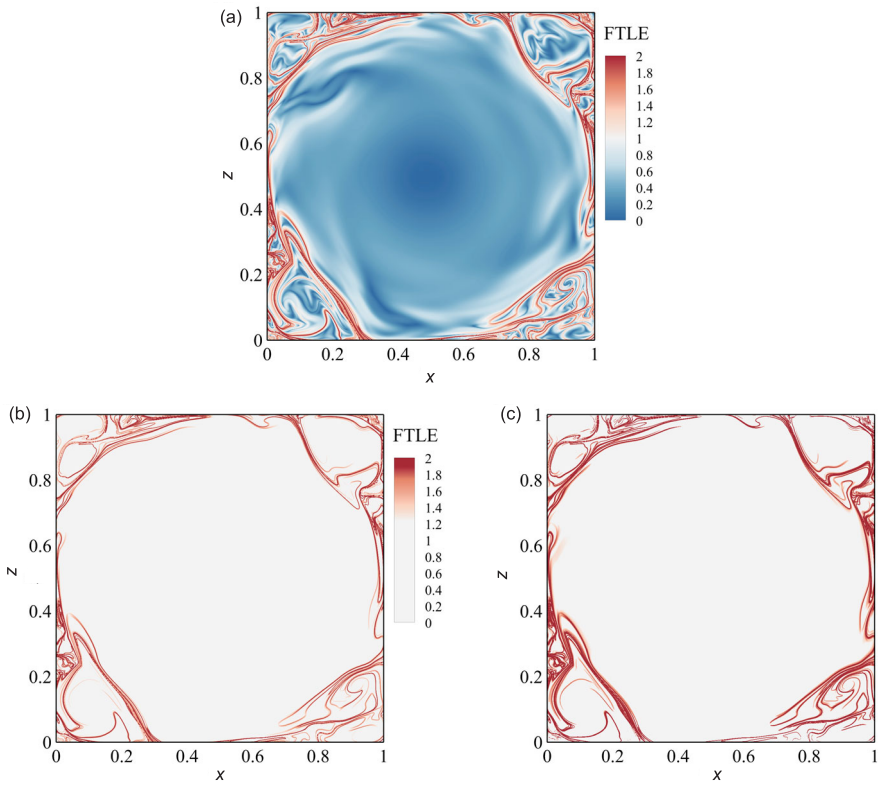

Figure 5 (a) Typical snapshots of FTLE fields at $Ra = 10^9$. (b) The LCSs identified according to the method used by Shadden et al. (c) The LCSs identified by applying the method of $\mathrm{FTLE}(x, y) - \langle \mathrm{FTLE} \rangle_x > c\mathrm{FTLE}_{\mathrm{r.m.s.}}$.

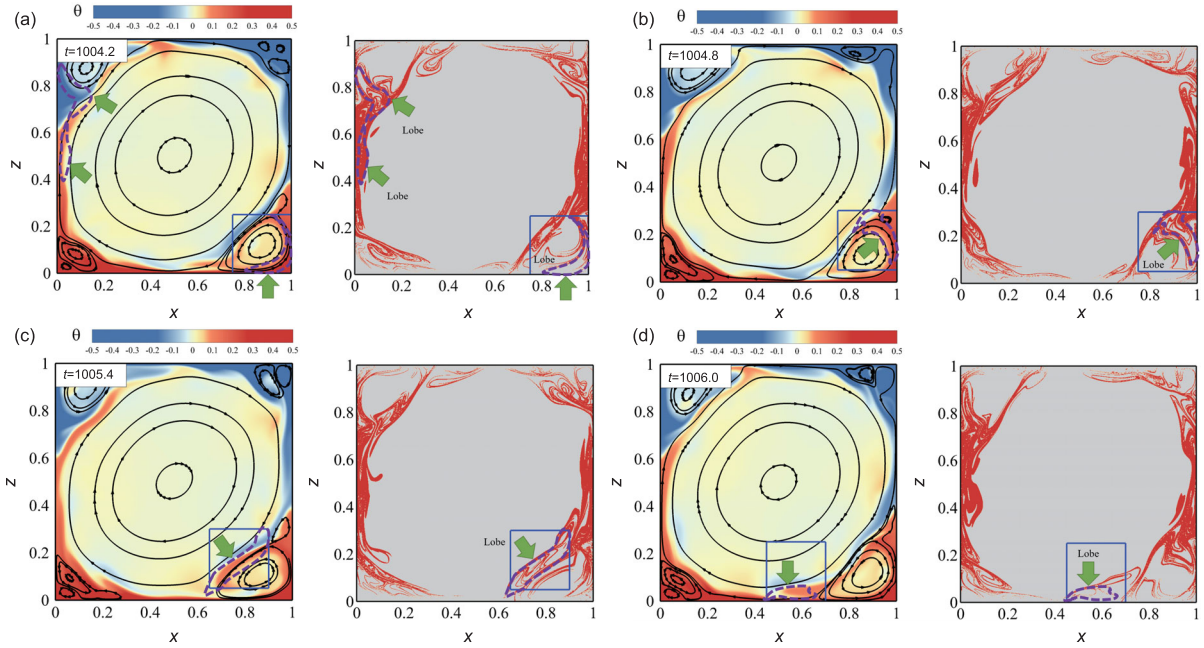

Figure 6 Time sequences of instantaneous temperature fields (color) and streamlines (black lines with arrows) at $Ra = 10^8$ are shown on the left panel of the subplot. The right panel of the subplot shows the LCSs (red lines) at the corresponding times. The lobe structures are marked in the figures with purple-dashed lines and green arrows, and their positions in the Eulerian fields are marked in the same way for the reader's observation. An evolution of the lobe structure in the blue frame shows its entrainment and detrainment process for heat. (a) $t = 1004.2$; (b) $t = 1004.8$; (c) $t = 1005.4$; (d) $t = 1006.0$.

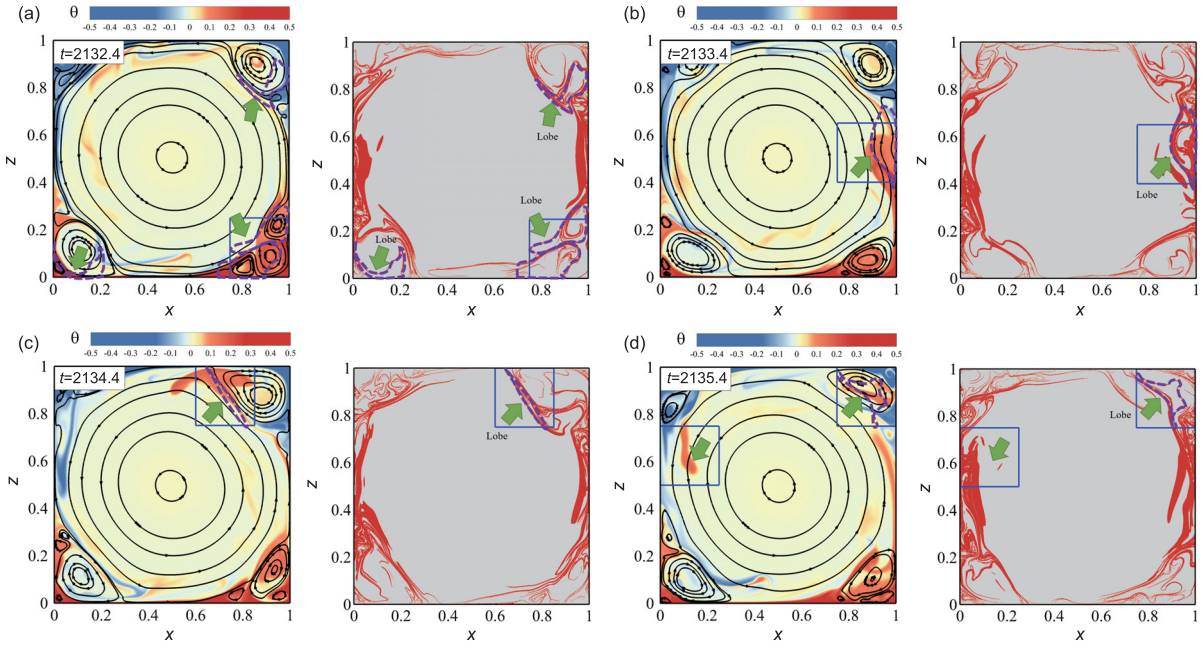

Figure 7 Time sequences of instantaneous temperature fields (color) and streamlines (black lines with arrows) at $Ra = 10^9$ are shown on the left panel of the subplot. The right panel of the subplot shows the LCSs (red lines) at the corresponding times. An evolution of the structures in the blue frame shows the vortex detached from the corner. (a) $t = 2132.4$; (b) $t = 2133.4$; (c) $t = 2134.4$; (d) $t = 2135.4$.

flow roll and further advected along the large-scale circulation (refer to Figure 6(d)). The periodic appearance of the lobe structures demonstrates the process of the entrainment/detrainment of fluids from the corner to the large-scale circulation, giving rise to heat exchange between them. It is worth noting that the lobe structures and their roles in the mass transfer have been studied briefly by Shadden et al. [40].

As Ra increases, the turbulence in the RB convection intensifies, and the corner-flow rolls become more unstable. Figure 7 shows snapshots of the instantaneous LCSs at $Ra = 10^9$. As shown in the figure, the main features of LCSs (including lobe structures and their entrainment and detrainment behavior) are similar to that at $Ra = 10^8$. We note that a part of the hot fluids carried by lobe structures in the corner rolls can be separated by LCSs, such that they eventually mix with the turbulent bulk (refer to Figure 7(d)). The other parts of hot fluids (plumes) remain in LCSs, move upwards and reach the top plate (refer to Figure 7(c)). A similar phenomenon is found for cold plumes near the upper plate (see the additional animation for more details).

From the preceding analysis of LCSs at different Ra, we conclude that the coherent structures obtained from the Lagrangian perspective can reveal more details of flow structures, mass transfer, and heat transport than those from the Eulerian perspective. Furthermore, LCSs, the representative structures of mass transfer, are responsible for the heat transport in RB convection.

3.2.1 *The spatial distributions of LCSs and plumes*

It is well-known that plumes are crucial to the formation of large-scale circulation and heat transport in RB convection. Recalling that the LCSs are recognized as the main structure responsible for heat transport in the last section, it is therefore essential to investigate the relationship between plumes and LCSs. To this aim, we compare the spatial distribution of plumes and LCSs. To identify thermal plumes, we follow the approach introduced by Zhang et al. [55] and Wang et al. [61]. Accordingly, the thermal plumes are defined as regions, where

$$\begin{aligned} &|\theta(x,y) - \langle\theta\rangle_x| > c\theta_{\text{r.m.s.}} \text{ and} \\ &\sqrt{RaPr}|w(x,y)\theta(x,y)| > cNu. \end{aligned} \tag{8}$$

The empirical constant c is set to 1.2, the same as that introduced by Zhang et al. [55]. The plume regions at $t = 2133.4$ in the case of $Ra = 10^9$ obtained by this criterion are shown in Figure 8(a). Here, the red (blue) color represents the hot (clod) plumes, and the corresponding LCSs are shown in Figure 8(b). The comparison of the spatial distributions of plumes and LCSs shows that plumes and LCSs are abundant near the sidewalls and overlap with each other in most places (refer to Figure 8(c)). To quantitatively describe the overlap, we calculate the mean ratios of the overlapping regions to plume and LCSs regions, respectively. As shown in Figure 9, both ratios are larger than 40%, indicating that most plumes

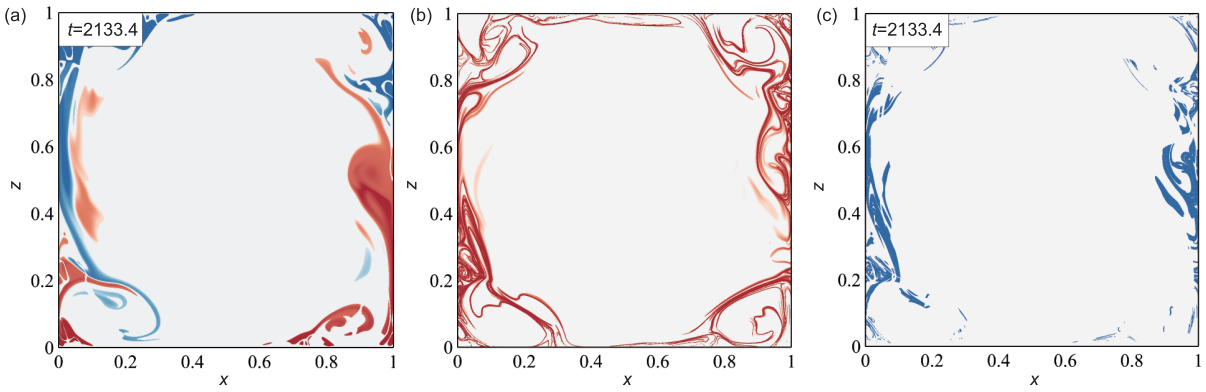

Figure 8 (a) Typical snapshots of the plume areas (color) at $Ra = 10^9$; (b) the corresponding instantaneous LCS areas (red); (c) overlap areas of plumes and LCSs (blue).

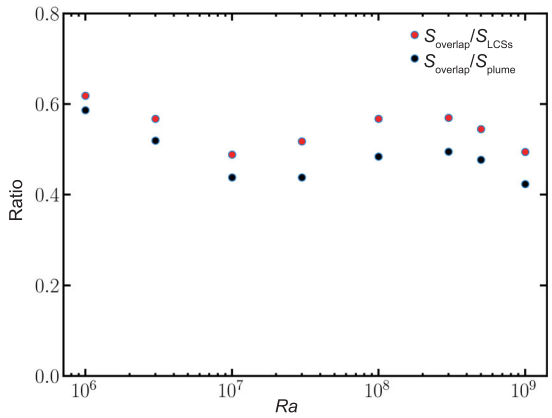

Figure 9 The time-averaged ratios of the overlap area to the LCS area (red dot) and the ratio of the overlap area (black dot) to the plume area as functions of Ra at $Pr = 0.7$, respectively.

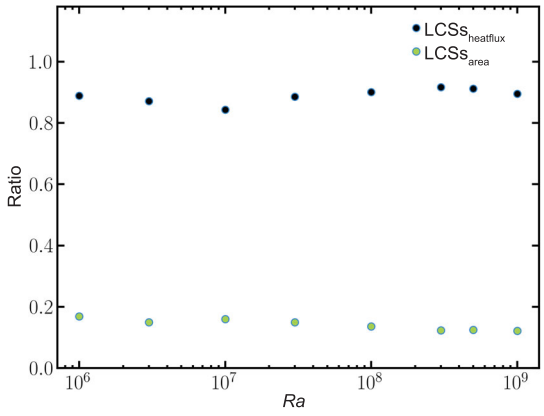

Figure 10 The time-averaged ratios of heat flux along the LCSs to the total heat flux (black dots) and the time-averaged ratios of LCS area to the cell area (green dots) as functions of Ra at $Pr = 0.7$.

may move along with LCSs. In this regard, we speculate that LCSs may be the main channel of heat transport.

3.2.2 *The relationship between LCSs and heat transport*

Furthermore, we quantify the vertical heat flux: $Q = \sqrt{RaPr}w(x,y)\theta(x,y)$ along the LCSs in RB convection. The mean ratios of heat flux by LCSs to the total flux for different Ra are shown in Figure 10, and the portions of the area occupied by LCSs over the entire cell area are shown. The most important finding from Figure 10 is that the heat flux ratios along the LCSs are larger than 85% of the total flux regardless of Ra. In contrast, the mean area ratios of LCSs to the cell are less than 20%. This confirms that LCSs are the main channels responsible for heat transport in RB convection.

3.2.3 *The relationship between LCSs and dissipation structures*

Viscous dissipation and thermal dissipation rates are two important quantities that have been extensively studied from the Eulerian perspective in the turbulent RB convection. We investigate the relationship between LCSs and these two dissipation rates from the Lagrangian perspective in this section. We question whether LCSs are also the main structures responsible for these two dissipation rates.

In order to answer this, we first calculate the viscous dissipation and thermal dissipation rates, which are respectively given by

$$\varepsilon_u = \frac{1}{2}\nu\Sigma_{i,j}\left[\frac{\partial u_j(x,t)}{\partial x_i} + \frac{\partial u_i(x,t)}{\partial x_j}\right]^2 \tag{9}$$

and

$$\varepsilon_\theta = \kappa\Sigma_i\left[\frac{\partial\theta(x,t)}{\partial x_i}\right]^2, \tag{10}$$

where $u(x,t)$ and $\theta(x,t)$ are the velocity and temperature fields; and ν and κ are the kinematic viscosity and thermal diffusivity of the fluid. The summation is calculated for i and j with $1 \to N_x$ and $1 \to N_z$.

Figure 11 shows typical snapshots of the instantaneous logarithmic fields for viscous dissipation rates ($\log_{10}\varepsilon_u$) and

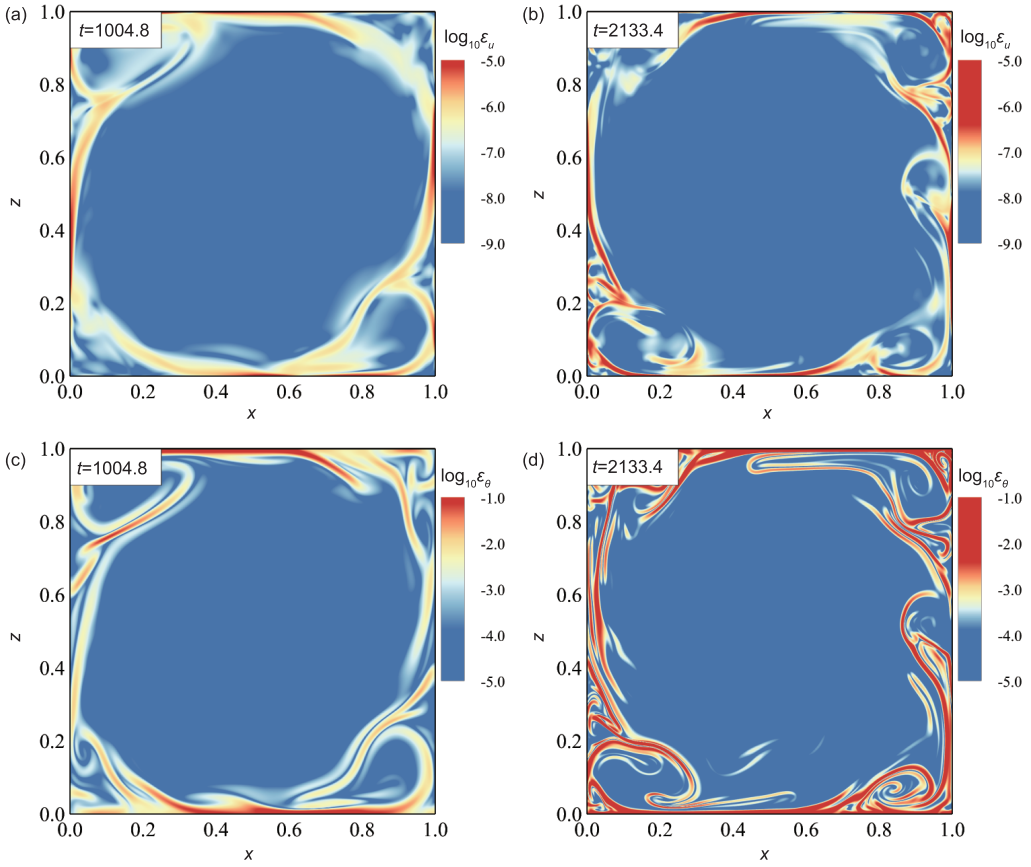

Figure 11 Typical snapshots of the instantaneous logarithmic fields of viscous $\log_{10}\varepsilon_u(x,z)$ ((a) and (b)) and thermal $\log_{10}\varepsilon_\theta(x,z)$ ((c) and (d)) dissipation rates at two different Ra numbers $Ra = 10^8$ ((a) and (c)) and $Ra = 10^9$ ((b) and (d)).

thermal dissipation rates ($\log_{10}\varepsilon_\theta$) for $Ra = 10^8$ and $Ra = 10^9$, respectively. The related FTLE and temperature fields correspond to Figures 6(b) and 7(b). As shown in these figures, the intense dissipation regions of ε_u and ε_θ almost coincide with hot and cold plume regions. It is also seen that the LCS regions are closely related to two intense dissipation regions.

Moreover, we quantify the contribution of LCSs to two dissipations at different Ra. The results are shown in Figure 12, where the time-averaged ratios of viscous dissipation rates along the LCSs to the total one (indicated by black dots) and that for thermal dissipation (indicated by red dots) are plotted as functions of Ra, respectively. As shown in Figure 12, the contributions of LCSs to viscous (thermal) dissipation rates are larger than 80% (60%) for all Ra considered in this paper. The higher contribution ratio of LCSs to viscous dissipation is because LCSs represent the most shearing regions [48]. Additionally, the lower contribution ratio of LCSs to thermal dissipation is caused by the partial overlapping of LCSs and plumes (refer to Figure 9). As shown in Figures 6, 7, 11, and 12, we conclude that LCSs are closely related to the high dissipative structures.

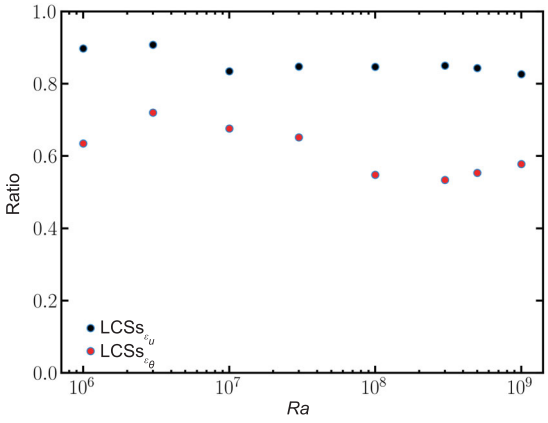

Figure 12 The time-averaged ratios of viscous dissipation rates along the LCSs to the total one (indicated by black dots) and that for thermal dissipation (indicated by red dots) are plotted as functions of Ra at $Pr = 0.7$, respectively.

4 Conclusions

In this paper, we have numerically investigated the role of LCSs in heat transport, viscous dissipation, and thermal dissi-

pation in RB convection with Ra ranging from 10^6 to 10^9 and Pr fixed at 0.7. First, we examine the self-organized coherent structures based on the Eulerian perspective and demonstrate the Nu-Ra scaling relationship, $Nu = 0.99Ra^{0.30\pm0.02}$, which is consistent with the previous studies. Second, we employ the FTLE method to identify LCSs to reveal how LCSs are intimately related to heat transport and large viscous and thermal dissipation events. The main results are summarized as follows.

(1) Based on LCSs, widespread lobe structures are found, which are related to the detrainment/entrainment process. We have particularly observed the periodicity of the lobe structures in the corner-flow rolls, corresponding to the heat exchange between the large-scale circulation and corner-flow rolls. Such information on heat exchange is not included in the traditional Eulerian analysis.

(2) By examining the relationship between LCSs and thermal plumes, we obtain that most plumes transport along the LCSs. In contrast, some plumes are exposed to the bulk and finally mix with the turbulent background. By virtue of LCSs, we have identified two distinct behaviors of thermal plumes.

(3) The ratio of the heat flux along the LCSs to the total value and occupied area of LCSs is calculated to quantitatively describe the role of LCSs in heat transport. The results show that the heat flux along the LCSs is larger than 85% of the total value, despite that LCSs only occupy less than 20% of the area. This indicates the significant role of LCSs in heat transport.

(4) By analyzing the viscous and thermal dissipations along the LCSs, we obtain that the viscous and thermal dissipation along the LCSs are larger than 80% and 60% of the total value, respectively. This suggests that LCSs are related to the strong viscous and thermal dissipation events.

Finally, we have demonstrated that analyzing LCSs is useful to deepen our understanding of heat transport. For example, the lobe structure is the hallmark feature as revealed using the Lagrangian approach, by which we elucidate how heat is exchanged between the large-scale circulation and the corner-flow rolls.

This work was supported by the National Natural Science Foundation of China (Grant Nos. 11732010, 92052201, 12072185, 91952102, 12032016).

1 Stevens B. Atmospheric moist convection. Annu Rev Earth Planet Sci, 2005, 33: 605–643
2 Thorpe S A. Recent developments in the study of ocean turbulence. Annu Rev Earth Planet Sci, 2004, 32: 91–109
3 Incropera F P. Convection heat transfer in electronic equipment cooling. J Heat Transfer, 1988, 110: 1097–1111
4 Chillà F, Schumacher J. New perspectives in turbulent Rayleigh-Bénard convection. Eur Phys J E, 2012, 35: 1–25
5 Ahlers G, Grossmann S, Lohse D. Heat transfer and large scale dynamics in turbulent Rayleigh-Bénard convection. Rev Mod Phys, 2009, 81: 503–537
6 Lohse D, Xia K Q. Small-scale properties of turbulent Rayleigh-Bénard convection. Annu Rev Fluid Mech, 2010, 42: 335–364
7 Ahlers G, Funfschilling D, Bodenschatz E. Transitions in heat transport by turbulent convection at Rayleigh numbers up to 10^{15}. New J Phys, 2009, 11: 123001
8 Lam S, Shang X D, Zhou S Q, et al. Prandtl number dependence of the viscous boundary layer and the Reynolds numbers in Rayleigh-Bénard convection. Phys Rev E, 2002, 65: 066306
9 Chillá F, Ciliberto S, Innocenti C, et al. Boundary layer and scaling properties in turbulent thermal convection. Il Nuovo Cimento D, 1993, 15: 1229–1249
10 Shishkina O, Wagner C. Local heat fluxes in turbulent Rayleigh-Bénard convection. Phys Fluids, 2007, 19: 085107
11 Stevens R J A M, Lohse D, Verzicco R. Prandtl and Rayleigh number dependence of heat transport in high Rayleigh number thermal convection. J Fluid Mech, 2011, 688: 31–43
12 Schmalzl J, Breuer M, Hansen U. On the validity of two-dimensional numerical approaches to time-dependent thermal convection. Europhys Lett, 2004, 67: 390–396
13 Malkus W V R. The heat transport and spectrum of thermal turbulence. Proc R Soc Lond A, 1954, 225: 196–212
14 Grossmann S, Lohse D. Scaling in thermal convection: A unifying theory. J Fluid Mech, 2000, 407: 27–56
15 Zhang Y Z, Sun C, Bao Y, et al. How surface roughness reduces heat transport for small roughness heights in turbulent Rayleigh-Bénard convection. J Fluid Mech, 2018, 836: R2
16 Zhu X, Jiang L F, Zhou Q, et al. Turbulent Rayleigh-Bénard convection in an annular cell. J Fluid Mech, 2019, 869: R5
17 Yang J L, Zhang Y Z, Jin T C, et al. The Pr-dependence of the critical roughness height in two-dimensional turbulent Rayleigh-Bénard convection. J Fluid Mech, 2021, 911: A52
18 Dong D L, Wang B F, Dong Y H, et al. Influence of spatial arrangements of roughness elements on turbulent Rayleigh-Bénard convection. Phys Fluids, 2020, 32: 045114
19 Kadanoff L P. Turbulent heat flow: Structures and scaling. Phys Today, 2001, 54: 34–39
20 Krishnamurti R, Howard L N. Large-scale flow generation in turbulent convection. Proc Natl Acad Sci USA, 1981, 78: 1981–1985
21 Qiu X L, Tong P. Large-scale velocity structures in turbulent thermal convection. Phys Rev E, 2001, 64: 036304
22 Xia K Q, Sun C, Zhou S Q. Particle image velocimetry measurement of the velocity field in turbulent thermal convection. Phys Rev E, 2003, 68: 066303
23 Xi H D, Lam S, Xia K Q. From laminar plumes to organized flows: The onset of large-scale circulation in turbulent thermal convection. J Fluid Mech, 1999, 503: 47–56
24 Sun C, Xi H D, Xia K Q. Azimuthal symmetry, flow dynamics, and heat transport in turbulent thermal convection in a cylinder with an aspect ratio of 0.5. Phys Rev Lett, 2005, 95: 074502
25 Xi H D, Zhou Q, Xia K Q. Azimuthal motion of the mean wind in turbulent thermal convection. Phys Rev E, 2006, 73: 056312
26 Brown E, Ahlers G. Rotations and cessations of the large-scale circulation in turbulent Rayleigh-Bénard convection. J Fluid Mech, 2006, 568: 351–386
27 Hunt J, Wray A, Moin P. Eddies, Streams, and Convergence Zones in Turbulent Flows. Center for Turbulence Research Report CTR-S88, 1988. 193
28 Bailon-Cuba J, Schumacher J. Low-dimensional model of turbulent Rayleigh-Bénard convection in a Cartesian cell with square domain. Phys Fluids, 2011, 23: 077101
29 Podvin B, Sergent A. Proper orthogonal decomposition investigation of turbulent Rayleigh-Bénard convection in a rectangular cavity. Phys Fluids, 2012, 24: 105106
30 Paul S, Verma M K. Proper orthogonal decomposition vs. fourier analysis for extraction of large-scale structures of thermal convection. In: Proceedings of Advances in Computation, Modeling and Control of Transitional and Turbulent Flows. Singapore: World Scientific, 2016.

433–441
31 Schmid P J. Dynamic mode decomposition of numerical and experimental data. J Fluid Mech, 2010, 656: 5–28
32 Schmid P J, Li L, Juniper M P, et al. Applications of the dynamic mode decomposition. Theor Comput Fluid Dyn, 2011, 25: 249–259
33 Huang Y X, Zhou Q. Counter-gradient heat transport in two-dimensional turbulent Rayleigh-Bénard convection. J Fluid Mech, 2013, 737: R3
34 Green M A, Rowley C W, Haller G. Detection of Lagrangian coherent structures in three-dimensional turbulence. J Fluid Mech, 2007, 572: 111–120
35 Ma X Y, Tang Z Q, Jiang N. Eulerian and Lagrangian analysis of coherent structures in separated shear flow by time-resolved particle image velocimetry. Phys Fluids, 2020, 32: 065101
36 Gasteuil Y, Shew W L, Gibert M, et al. Lagrangian temperature, velocity, and local heat flux measurement in Rayleigh-Bénard convection. Phys Rev Lett, 2007, 99: 234302
37 Hadjighasem A, Farazmand M, Blazevski D, et al. A critical comparison of Lagrangian methods for coherent structure detection. Chaos, 2017, 27: 053104
38 Suara K, Khanarmuei M, Ghosh A, et al. Material and debris transport patterns in Moreton Bay, Australia: The influence of Lagrangian coherent structures. Sci Total Environ, 2020, 721: 137715
39 Karrasch D, Keller J. A geometric heat-flow theory of Lagrangian coherent structures. J Nonlinear Sci, 2020, 30: 1849–1888
40 Shadden S C, Dabiri J O, Marsden J E. Lagrangian analysis of fluid transport in empirical vortex ring flows. Phys Fluids, 2006, 18: 047105
41 Procaccia I. Go with the flow. Nature, 2001, 409: 993–995
42 Haller G, Yuan G. Lagrangian coherent structures and mixing in two-dimensional turbulence. Physica D, 2000, 147: 352–370
43 Belkin M, Niyogi P. Laplacian eigenmaps for dimensionality reduction and data representation. Neural Computation, 2003, 15: 1373–1396
44 Farazmand M, Haller G. Polar rotation angle identifies elliptic islands in unsteady dynamical systems. Physica D, 2016, 315: 1–12
45 Mathur M, Haller G, Peacock T, et al. Uncovering the Lagrangian skeleton of turbulence. Phys Rev Lett, 2007, 98: 144502
46 Haller G, Sapsis T. Lagrangian coherent structures and the smallest finite-time Lyapunov exponent. Chaos, 2011, 21: 023115
47 Peacock T, Haller G. Lagrangian coherent structures: The hidden skeleton of fluid flows. Phys Today, 2013, 66: 41–47
48 Haller G. Lagrangian coherent structures. Annu Rev Fluid Mech, 2015, 47: 137–162
49 Haller G. Lagrangian coherent structures from approximate velocity data. Phys Fluids, 2002, 14: 1851–1861
50 Shadden S C, Lekien F, Marsden J E. Definition and properties of Lagrangian coherent structures from finite-time Lyapunov exponents in two-dimensional aperiodic flows. Physica D, 2005, 212: 271–304
51 He G S, Pan C, Feng L H, et al. Evolution of Lagrangian coherent structures in a cylinder-wake disturbed flat plate boundary layer. J Fluid Mech, 2016, 792: 274–306
52 Li S, Jiang N, Yang S Q, et al. Coherent structures over riblets in turbulent boundary layer studied by combining time-resolved particle image velocimetry (TRPIV), proper orthogonal decomposition (POD), and finite-time Lyapunov exponent (FTLE). Chin Phys B, 2018, 27: 104701
53 Schneide C, Stahn M, Pandey A, et al. Lagrangian coherent sets in turbulent Rayleigh-Bénard convection. Phys Rev E, 2019, 100: 053103
54 du Puits R, Li L, Resagk C, et al. Turbulent boundary layer in high Rayleigh number convection in air. Phys Rev Lett, 2014, 112: 124301
55 Zhang Y, Zhou Q, Sun C. Statistics of kinetic and thermal energy dissipation rates in two-dimensional turbulent Rayleigh-Bénard convection. J Fluid Mech, 2017, 814: 165–184
56 Bao Y, Chen J, Liu B F, et al. Enhanced heat transport in partitioned thermal convection. J Fluid Mech, 2015, 784: R5
57 Chen J, Bao Y, Yin Z X, et al. Theoretical and numerical study of enhanced heat transfer in partitioned thermal convection. Int J Heat Mass Transfer, 2017, 115: 556–569
58 Zhang Y Z, Xia S N, Dong Y H, et al. An efficient parallel algorithm for DNS of buoyancy-driven turbulent flows. J Hydrodyn, 2019, 31: 1159–1169
59 Sugiyama K, Ni R, Stevens R J A M, et al. Flow reversals in thermally driven turbulence. Phys Rev Lett, 2010, 105: 034503
60 Zhang Y, Huang Y X, Jiang N, et al. Statistics of velocity and temperature fluctuations in two-dimensional Rayleigh-Bénard convection. Phys Rev E, 2017, 96: 023105
61 Wang B F, Zhou Q, Sun C. Vibration-induced boundary-layer destabilization achieves massive heat-transport enhancement. Sci Adv, 2020, 6: eaaz8239